

Characterizing and predicting the magnetic environment leading to solar eruptions

Tahar Amari¹, Aurélien Canou¹ & Jean-Jacques Aly²

The physical mechanism responsible for coronal mass ejections has been uncertain for many years, in large part because of the difficulty of knowing the three-dimensional magnetic field in the low corona¹. Two possible models have emerged. In the first, a twisted flux rope moves out of equilibrium or becomes unstable, and the subsequent reconnection then powers the ejection^{2–5}. In the second, a new flux rope forms as a result of the reconnection of the magnetic lines of an arcade (a group of arches of field lines) during the eruption itself⁶. Observational support for both mechanisms has been claimed^{7–9}. Here we report modelling which demonstrates that twisted flux ropes lead to the ejection, in support of the first model. After seeing a coronal mass ejection, we use the observed photospheric magnetic field in that region from four days earlier as a boundary condition to determine the magnetic field configuration. The field evolves slowly before the eruption, such that it can be treated effectively as a static solution. We find that on the fourth day a flux rope forms and grows (increasing its free energy). This solution then becomes the initial condition as we let the model evolve dynamically under conditions driven by photospheric changes (such as flux cancellation). When the magnetic energy stored in the configuration is too high, no equilibrium is possible and the flux rope is ‘squeezed’ upwards. The subsequent reconnection drives a mass ejection.

Coronal mass ejections (CMEs) are large-scale eruptive events in the solar atmosphere that could have impact¹⁰ on satellites and ground-based power generation. Theoretical models^{11,12} of their origins use a specific coronal configuration whose evolution is computed from a given initial state. A global disruption leading to the ejection of a twisted flux rope identified with a CME—through an overlying arcade—is then found to occur. The rope may be present in the initial state as a stable equilibrium structure; as an unstable or nearly unstable equilibrium structure that evolves freely at later times^{13,14}; or as a subphotospheric structure that is forced by buoyancy to emerge through the solar surface into the corona, where it expands^{15,16}. Alternatively, the initial state may simply be one or more arcades evolving through photospheric shearing motions, the rope being produced during the disruption itself⁶.

The following method can be used to determine which, if either, of these situations describes an actual eruptive event. In a first step, consider the pre-eruptive phase during which the coronal magnetic field can be assumed to evolve slowly through a sequence of equilibrium force-free configurations. Under this quite reasonable assumption, the field evolution can be computed from successive measurements made at the photospheric level, and the presence or absence of a twisted flux rope can be assessed. The problem is, however, very difficult, and safe conclusions can be reached only using a very accurate numerical code suited for force-free magnetic fields as well as high-resolution, low-noise measurements. In a second step, the configuration obtained slightly before the eruption is used as the initial state in a dynamical magnetohydrodynamics (MHD) code along with boundary conditions mimicking the physical photospheric processes that makes the coronal field evolve. It is then possible to look for a disruption of the configuration having properties comparable to the observed ones. It is worth noticing that this

method, once successfully tested against well-documented past events, could be applied to forecast the eruption of an active region (the aim of studying space weather), the eruptive power at any given time being predicted by reconstructing the field at that time and using it in a dynamical code as indicated above.

Here we apply this method to US National Oceanic and Atmospheric Administration (NOAA) active region 10930 (AR10930), which crossed the solar disk during the first half of December 2006. This choice is motivated by two factors. First, the region clearly exhibits most of the features usually associated with eruptive behaviour. Second, the spectropolarimeter of the Solar Optical Telescope (SOT) on board the satellite Hinode¹⁷ has provided a series of high-precision measurements of the photospheric field around the time of the eruption. This prompted many groups to study this region, but hitherto none of them has provided the complete, fully data-driven picture (including both the pre-eruptive and the eruptive phases) that we are seeking here. Most of them^{18–21} (see Methods for supplementary references) have concentrated on the reconstruction problem, without showing unambiguously the presence of the pre-eruptive rope. As for the dynamical evolution of the region, an MHD computation leading to an eruption has been proposed²², but it starts from an initial state in which a twisted flux tube with adequate properties has been forced to emerge into the region rather than being obtained from a reconstruction based on the only observational magnetic data (a similar calculation, but with the tube introduced by the insertion method, was recently done for another region¹⁴). And the mechanism of the eruption has been discussed by comparing some observational features with the results of a simple theoretical model in which a twisted rope is forced to erupt into a highly sheared arcade²³.

To set the stage, we note that the evolution of NOAA AR10930 was associated with the emergence of a positive-polarity sunspot²⁴. This complex process involved translational and apparent rotational motions of the sunspot of the southern region, and led to the elongation of the spots, which is the signature of an emerging twisted rope²⁵ (Supplementary Video 1). A series of flares were observed during the transit of AR10930. An X3.4 two-ribbon flare occurred on December 13 from 2:14 UT to 2:57 UT, with its peak in soft X-rays at 2:40 UT. It had brightenings that started around the magnetic polarity inversion line between the two main spots, which then moved apart. It was followed by a halo-like CME with the potential to create a geomagnetic storm, which was observed using the C2 coronagraph on the Large Angle and Spectrometric Coronagraph Experiment on board NASA’s Solar and Heliospheric Observatory (SOHO) at 2:54 UT. The total energy (kinetic plus gravitational) released during this major event was estimated²⁶ to be $(1.4–4.5) \times 10^{32}$ erg.

We compute the magnetic environment above AR10930 from December 9 to December 12 at 20:30 UT by using our extrapolation code XTRAPOL²⁷, with the required boundary conditions being provided by vector magnetograms taken from the scans of the Hinode/SOT spectropolarimeter¹⁷. Several important features appear in the reconstructed states. As the evolution proceeds from day D–4 (four days before the eruption) to day D (the date of the eruption) as a consequence of flux emergence, the field suffers a change from an arcade-like topology

¹Centre de Physique Théorique, Ecole Polytechnique, CNRS, F-91128 Palaiseau Cedex, France. ²AIM, Unité Mixte de Recherche CEA, CNRS, Université Paris VII, UMR 7158, Centre d’Etudes de Saclay, F-91191 Gif sur Yvette Cedex, France.

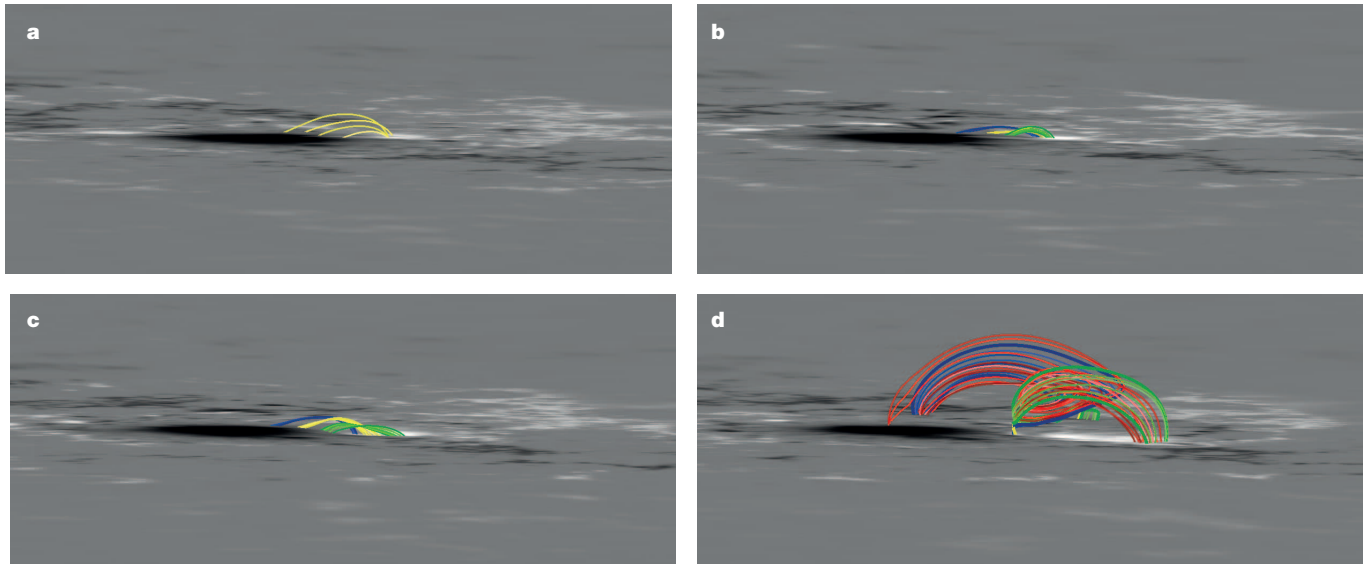


Figure 1 | Magnetic field evolution during the days before major eruption day D. Selected field lines of some magnetic configurations obtained by reconstructing the coronal magnetic field around the eruption site using vector magnetograms from Hinode/SOT and a static MHD model. Energy builds up slowly, with field lines shearing several days before the eruption, during the emergence of the positive-polarity sunspot (white) into the background of an

older, negative-polarity sunspot (black). **a**, Four days before the eruption (D-4); **b**, D-3; **c**, D-2; **d**, D-1. The magnetic field becomes progressively sheared in between the two spots, until a large twisted flux rope has formed on D-1. Colour code: yellow, sheared arcades; blue and green, J-shaped loops; red, largely twisted field lines.

to a rope-like one (Fig. 1 and Supplementary Video 2). On D-2, the model produces two J-shaped structures surrounding a highly sheared inner arcade with almost no twist (Fig. 1c), similar to those produced in idealized models driven by flux cancellation²⁻⁴. On D-1, we also use our new global reconstruction code MESHMHD²⁸ along with composite photospheric data from three instruments, which allows us to resolve both small- and large-scale features (Extended Data Fig. 1). The active region from which the eruption originates is shown to be well isolated and not interacting with neighbouring active regions. A flux rope with a twist greater than 2π has formed. There is evidence that the tube has a hyperbolic structure, which is known from previous models²⁹ to be the signature of a slow flux and magnetic helicity transfer by magnetic reconnection from the photosphere to the twisted rope (Extended Data Fig. 2). Some magnetic helicity appears to have been redistributed into the rope, resulting in an increase of its twist during the period from D-2 to D-1. The structure of the electric currents flowing along it on D-1 is shown in Extended Data Fig. 3.

The accuracy of our computed configurations is attested to by the very good agreement existing between some of their characteristic features and coronal observations. In particular, the magnetic lines of the twisted rope (which coincide with the lines of the current density in our force-free reconstructions) exhibit dips at the precise location of the filament of cool material observed in H α emission using the spectroheliograph at the Paris-Meudon Observatory (Fig. 2c, d), and they are well aligned with both the X-ray data from the Hinode X-ray Telescope (XRT) (Fig. 2b) and the extreme-ultraviolet data from the SOHO Extreme Ultraviolet Imaging Telescope (EIT) (Extended Data Fig. 4). The latter also show a good alignment with the magnetic lines of some outer parts of the region. Furthermore, the series of reconstructions made from D-4 to D-1 show that the rope is forming by emergence from below the photosphere as the southern spot of the observed active region is emerging, with a very good correlation with the observed photospheric tongues (Fig. 2a and Supplementary Video 2).

During the four modelled days, the magnetic energy increases considerably. Up to four days before the eruption, the amount of accumulated free energy—that is, the part of the energy above that of the current-free magnetic field—is too low to power it. At D-2, the free energy enters the ‘possible’ zone of eruption but is still close to the lower-bound estimate.

older, negative-polarity sunspot (black). **a**, Four days before the eruption (D-4); **b**, D-3; **c**, D-2; **d**, D-1. The magnetic field becomes progressively sheared in between the two spots, until a large twisted flux rope has formed on D-1. Colour code: yellow, sheared arcades; blue and green, J-shaped loops; red, largely twisted field lines.

On D-1, the free magnetic energy becomes large enough to power the observed major eruption (Fig. 3a). A few hours before the eruption, the energy is close to that of a particular partially open field, B_{so} , whose importance has been stressed in previous idealized simulations⁴ (Methods). Magnetostatic equilibrium is no longer possible when the energy of B_{so} is exceeded, a phenomenon known as catastrophic loss of equilibrium.

We take the low-corona configurations computed on D-2 and D-1, respectively, as initial conditions of our numerical dynamical MHD code METEOSOL^{2-4,30}. The static solution evolves under the effects of a flux decrease² (associated with flux cancellation), gas motion characteristic of a sunspot ‘moat flow’⁴, or photospheric turbulent diffusion^{3,5}.

We find that the magnetic configuration corresponding to the December 11, 10:00 UT (D-2) data does not lead to a major disruption, but rather to relaxation to a new equilibrium. Pushing the evolution further, however, results in the formation of a small twisted rope that eventually suffers a small, confined eruption. We do not get a major disruption because not enough flux has been transferred to the rope at D-2, with the available free energy staying well below the loss of equilibrium threshold. This shows that even at an early stage during the build-up of the active region the configuration has already acquired some eruptive potential (even if small).

The situation is different when the evolution is computed with the data of D-1 at 20:30 UT. The twisted rope has already formed and contains a large amount of flux and electric current, and it is found to erupt, with the magnetic lines exhibiting a shape very similar to that generally reported when an eruption is observed on the solar limb (Fig. 4c, d). The overall configuration suffers a major disruption (Fig. 4a, b), which we argue explains the occurrence of the eruption of December 13, 2:40 UT. At the time of disruption, the magnetic energy of the configuration becomes of the same order as the critical energy (that of B_{so}). We interpret this as meaning that the field has suffered a loss of equilibrium, where the magnetic tension force no longer balances the magnetic pressure force.

The onset of an eruption has been proposed^{5,13,14} to occur when a rope reaches an altitude at which an index n characterizing the vertical decay of the horizontal component of the current-free field exceeds a critical value $n_c \approx 3/2$ (the ‘torus instability criterion’). We have computed n for our configuration of day D-1 and found that n is close to n_c (Fig. 3c-e).

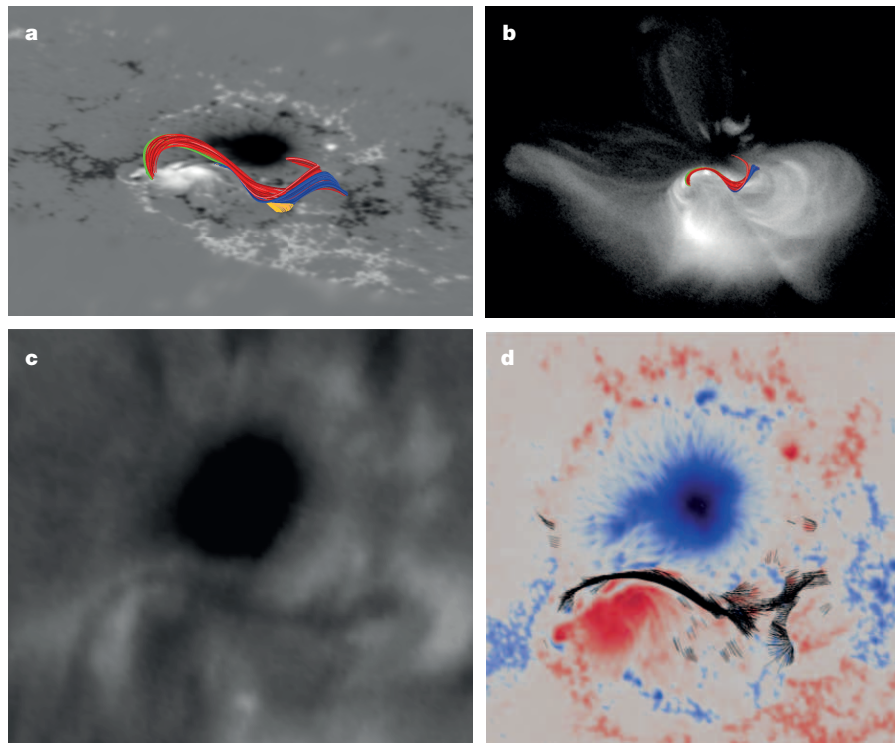


Figure 2 | Twisted flux rope before the major eruption. Selected field lines of the reconstructed magnetic configuration of December 12, 20:30 UT (D-1), with the same colour code as in Fig. 1. **a**, A large rope consisting of several components sits between the two spots and is seen to have accumulated a large amount of twist (about 2.25π). The hyperbolic nature of the rope (field lines bifurcating with an X-type topology) is detailed in Extended Data Fig. 2. **b**, Good agreement of the shape of some computed field lines with X-ray data from Hinode/XRT. **c**, H α data from the spectroheliograph at the Paris-Meudon Observatory reveals that a filament (darker) extends in the atmosphere between the two spots. **d**, The filament shown in **c** coincides with the locations of the dips in the computed magnetic field (shown as black segments and seen from the same vantage point as in **c**) where cool material can sit and be supported against gravity by the magnetic force.

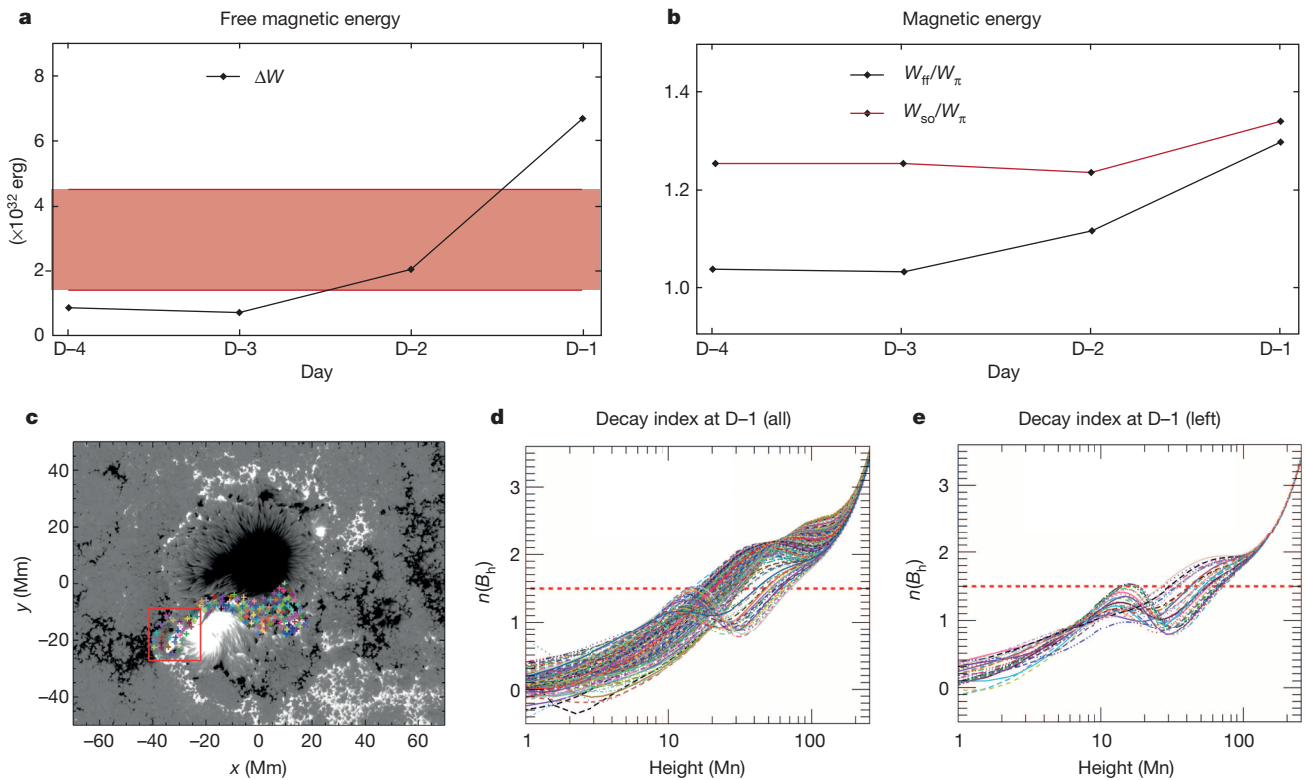


Figure 3 | Accumulation of magnetic energy. **a**, Evolution of the free magnetic energy (black curve) during the four days before the major eruption. The actual energy of the major eruption lies in the red zone, defined by upper and lower limits estimated from the observations. **b**, Magnetic energy W_{ff} of the configuration (black curve) and theoretical magnetic energy upper bound W_{so} , beyond which equilibrium is no longer possible (red curve), in units of the magnetic energy W_{π} of the (minimum-energy) current-free magnetic configuration having the same B_z distribution on the photosphere. During the last day (D-1), the magnetic energy of the configuration comes closer to this

bound. **c**, Normal component of the magnetic field at D-1. The coloured crosses indicate a set of points selected along the photospheric projection of the twisted rope. **d**, Variations with altitude of the index n characterizing the decay of the horizontal component of the current-free magnetic field B_h above each of the coloured points in **c**. The red dashed line corresponds to the critical value $n_c \approx 3/2$, beyond which the rope is ejected according to the torus instability criterion. **e**, Variations in n for a subset of points lying inside the red rectangle in **c**, which is located on the left side of the southern spot.

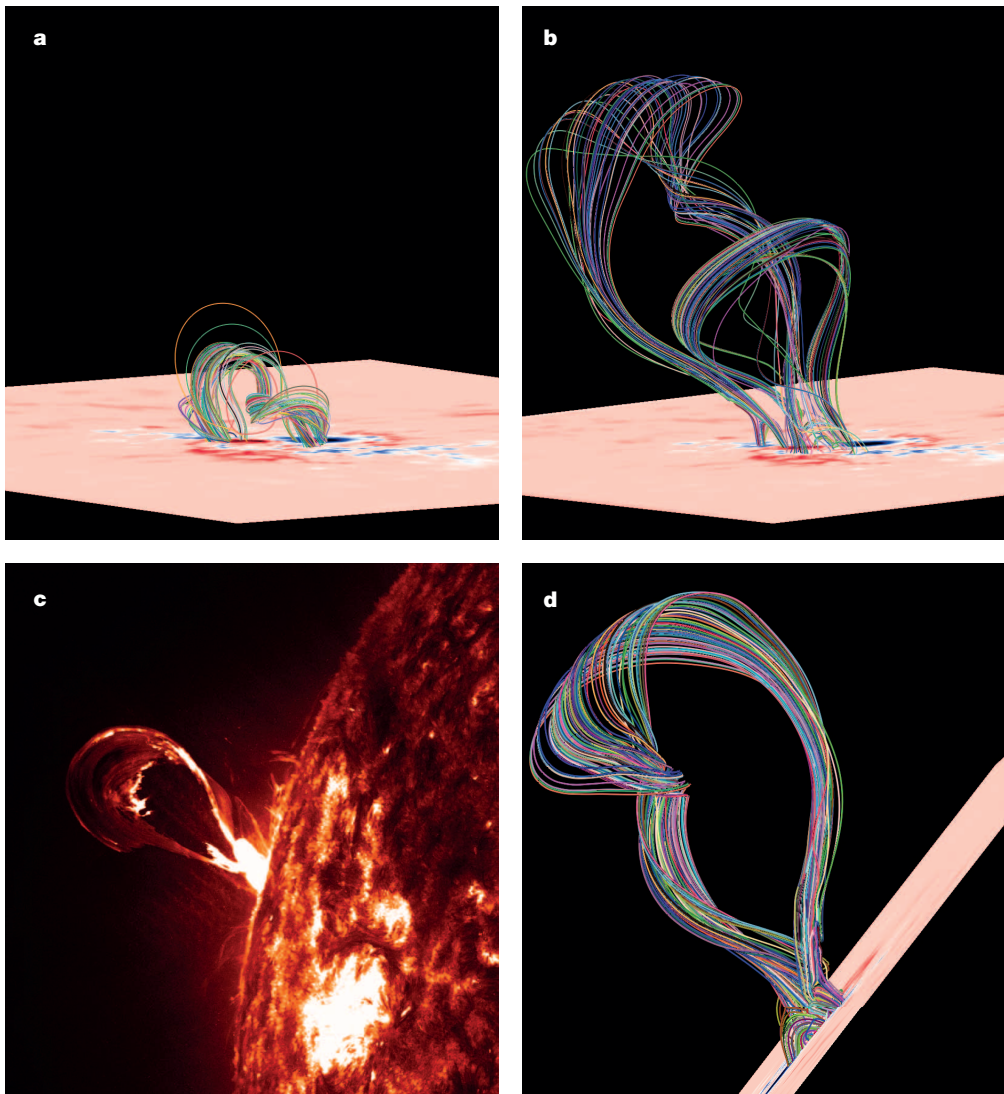


Figure 4 | Evolution and eruption of the twisted flux rope. Selected field lines of some configurations obtained after an evolution driven by photospheric changes, with the configuration of December 12, 20:30 UT being taken as the initial condition. **a**, In accordance with Fig. 3b, at around 20:30 UT the configuration is almost out of equilibrium and the rope rapidly rises. **b**, Sometime later, it erupts through the arcades that were able to confine it several hours before. **c**, Observed typical shape exhibited by eruptions on the solar limb (image taken at a wavelength of 304 Å by SDO/AIA on 2012 October 14, at 2:32 UT; courtesy of NASA/SDO and the AIA, EVE and HMI science teams). **d**, Modelled appearance of the major eruption of December 13, projected onto the solar limb, showing agreement with the typical shape shown in **c** (for convenience, the arcades have been removed).

There is then an agreement between our energetic onset criterion and the torus instability one. Moreover, n is closer to n_c in the region near the left side of the southern spot, which might explain the asymmetric ejection of the rope whose eruption is stronger above that region (Fig. 3e). Finally, during the MHD phase of the rising of the rope, most of it eventually reaches a height at which $n = n_c$. It has been suggested¹⁴ that the onset of an eruption may be also characterized in terms of a flux criterion, with the rope being ejected once the ratio of its axial flux to the flux through the main part of the active region becomes too large. We find that this parameter is equal to 15.3% at $D - 1$.

Online Content Methods, along with any additional Extended Data display items and Source Data, are available in the online version of the paper; references unique to these sections appear only in the online paper.

Received 22 July; accepted 29 August 2014.

- Cargill, P. Coronal magnetism: difficulties and prospects. *Space Sci. Rev.* **144**, 413–421 (2009).
- Amari, T., Luciani, J.-F., Mikic, Z. & Linker, J. A twisted flux rope model for coronal mass ejection and two-ribbon flares. *Astrophys. J.* **529**, L49–L52 (2000).
- Amari, T., Luciani, J.-F., Aly, J.-J., Mikic, Z. & Linker, J. Coronal mass ejection: initiation, helicity and flux ropes. II. Turbulent diffusion driven evolution. *Astrophys. J.* **595**, 1231–1250 (2003).
- Amari, T., Aly, J.-J., Luciani, J.-F., Mikic, Z. & Linker, J. Coronal mass ejection initiation by converging photospheric flows: toward a realistic model. *Astrophys. J.* **742**, L27 (2011).
- Aulanier, G., Török, T., Démoulin, P. & DeLuca, E. E. Formation of torus-unstable flux ropes and electric currents in erupting sigmoids. *Astrophys. J.* **708**, 314–333 (2010).
- Antiochos, S. K., DeVore, C. R. & Klimchuk, J. A. A model for coronal mass ejection. *Astrophys. J.* **510**, 485–493 (1999).
- Howard, T. A. & DeForest, C. E. Inner heliospheric flux rope evolution via imaging of coronal mass ejections. *Astrophys. J.* **746**, 64–76 (2012).
- Cheng, X. *et al.* Tracking the evolution of a coherent magnetic flux rope continuously from the inner to the outer corona. *Astrophys. J.* **780**, 28 (2014).
- Kumar, P. & Innes, D. E. Multiwavelength observations of an eruptive flare: evidence for blast wave and break out. *Sol. Phys.* **288**, 255–268 (2013).
- Hapgood, M. Prepare for the coming space weather storm. *Nature* **484**, 311 (2012).
- Forbes, T. G. *et al.* CME theory and model. *Space Sci. Rev.* **123**, 251–302 (2006).
- Shibata, K. & Magara, T. Solar flares: magnetohydrodynamic processes. *Living Rev. Sol. Phys.* **8**, 6 (2011).
- Kliem, B. & Török, T. Torus instability. *Phys. Rev. Lett.* **96**, 255002 (2006).
- Kliem, B. *et al.* Magnetohydrodynamic modeling of the solar eruption on 2010 April 8. *Astrophys. J.* **779**, 129 (2013).
- Fan, Y. The emergence of a twisted flux tube into the solar atmosphere: sunspot rotations and the formation of a coronal flux rope. *Astrophys. J.* **697**, 1529–1542 (2009).
- Roussev, I. I. *et al.* Explaining fast ejection of plasma and exotic X-ray emission from the solar corona. *Nature Phys.* **8**, 845–849 (2012).
- Kosugi, T. *et al.* The Hinode (Solar-B) mission: an overview. *Sol. Phys.* **243**, 3–17 (2007).
- Schrijver, C. J. *et al.* Nonlinear force-free field modeling of a solar active region around the time of a major flare and coronal mass ejection. *Astrophys. J.* **675**, 1637–1644 (2008).
- Guo, Y., Ding, M. D., Wiegmann, T. & Li, H. 3D magnetic field configuration of the 2006 December 13 flare extrapolated with the optimization method. *Astrophys. J.* **679**, 1629–1635 (2008).
- Jing, J., Wiegmann, T., Suematsu, Y., Kubo, M. & Wang, H. Changes of magnetic structure in three dimensions associated with the X3.4 flare of 2006 December 13. *Astrophys. J.* **676**, L81–L84 (2008).

21. Inoue, S., Kusano, K., Magara, T., Shiota, D. & Yamamoto, T. T. Twist and connectivity of magnetic field lines in the solar active region NOAA 10930. *Astrophys. J.* **738**, 161 (2011).
22. Fan, Y. A magnetohydrodynamic model of the 2006 December 13 eruptive flare. *Astrophys. J.* **740**, 68 (2011).
23. Kusano, K. *et al.* Magnetic structures triggering solar flares and coronal mass ejections. *Astrophys. J.* **760**, 31 (2012).
24. Min, S. & Chae, J. The rotating sunspot in AR 10930. *Sol. Phys.* **258**, 203–217 (2009).
25. Luoni, M. L. *et al.* Twisted flux tube emergence evidenced in longitudinal magnetograms: magnetic tongues. *Sol. Phys.* **270**, 45–74 (2011).
26. Ravindra, B. & Howard, T. A. Comparison of energies between eruptive phenomena and magnetic field in AR 10930. *Bull. Astron. Soc. India* **38**, 147–163 (2010).
27. Amari, T., Boulmezaoud, T. Z. & Aly, J.-J. Well posed reconstruction of the solar coronal magnetic field. *Astron. Astrophys.* **446**, 691–705 (2006).
28. Amari, T. *et al.* in *Proc. ASP Conf. Ser. 459* (eds Pogorelov, N. V., Font, J. A., Audit, E. & Zank, G. P.) 189 (Astronomical Society of the Pacific, 2012).
29. Titov, V. S. & Hornig, G. Magnetic connectivity of coronal fields: geometrical versus topological description. *Adv. Space Res.* **29**, 1087–1092 (2002).
30. Amari, T., Luciani, J. F. & Joly, P. A preconditioned semi implicit scheme for magnetohydrodynamics equations. *SIAM J. Sci. Comput.* **21**, 970–986 (1999).

Supplementary Information is available in the online version of the paper.

Acknowledgements The numerical simulations described in this paper were performed on the IBM x3750 of the IDRIS institute of the Centre National de la Recherche Scientifique (CNRS). We thank the Centre National d'Etudes Spatiales (CNES) for its financial support. Hinode is a Japanese mission developed and launched by ISAS/JAXA, with NAOJ as domestic partner and NASA and STFC (UK) as international partners. It is operated by these agencies in co-operation with ESA and NSC (Norway). H α data used in this study were provided by Paris-Meudon Observatory, X-ray data came from Hinode/XRT and extreme-ultraviolet data came from SOHO/EIT.

Author Contributions T.A. and A.C. planned and performed the various calculations, and discussed the analysis with J.-J.A. The manuscript was written by T.A. and J.-J.A. with feedback from A.C.

Author Information Reprints and permissions information is available at www.nature.com/reprints. The authors declare no competing financial interests. Readers are welcome to comment on the online version of the paper. Correspondence and requests for materials should be addressed to T.A. (amari@cph.t.polytechnique.fr).

METHODS

The basic strategy that we have adopted is the following: first, we model the pre-eruptive phase through a series of reconstructions of the field (assumed to be in force-free equilibrium), with the needed boundary conditions being computed from the observational data. Second, we predict the evolution of the field during the eruptive phase by using the last obtained equilibrium as the initial condition of a simulation done with a full MHD code. The physical results we get depend on both the quality of the data used and the mathematical efficiency of the method.

Magnetic environment model at equilibrium. The magnetic field \mathbf{B} can be measured only in the photosphere, but we need a coronal value. During the occurrence of an eruptive event, \mathbf{B} and the highly conducting, low- β plasma in which it is embedded evolve very slowly. \mathbf{B} can thus be considered as being at each time t in an equilibrium force-free state in which it obeys the set of equations³¹

$$\nabla \times \mathbf{B} = \alpha(r)\mathbf{B} \quad (1)$$

$$\nabla \cdot \mathbf{B} = 0 \quad (2)$$

$$\mathbf{B} \cdot \nabla \alpha(r) = 0 \quad (3)$$

where $\alpha(r)$ is some scalar function of position r . Equation (3) (which is a consequence of equations (1) and (2)) implies that α keeps a constant value along any field line. One is thus led to set up the ‘reconstruction problem’: to determine in the part Ω of the corona above an active region a magnetic field \mathbf{B} satisfying as closely as possible the following conditions: (1) it is a finite-energy, force-free magnetic field in Ω and (2) it matches on the lower boundary S of Ω the value \mathbf{B}^{phot} provided by the measurements done at the photospheric level³¹. The reason why we added the restrictive qualification ‘as closely as possible’ is that there is generally no field \mathbf{B} satisfying conditions (1) and (2) simultaneously. The raw data can be ‘preprocessed’³² to try to diminish the incompatibility between both requirements, but it cannot be totally suppressed. The best one can do is to set up a resolution scheme which is well-posed, in the sense that it leads to a unique solution that is stable with respect to small changes in the data.

Several methods³¹ have been developed to treat the reconstruction problem, each one using the data in a specific way and defining a particular environment model, and it is important when one studies a particular active region to compare the results furnished by various approaches¹⁸. One should also compare these results with characteristic observational features of the region (like the presence of a filament at some particular location).

To reconstruct the coronal field, we use a Grad–Rubin type method that solves a mixed hyperbolic–elliptic boundary-value problem for the force-free function α and for the field \mathbf{B} (ref. 27). This method is based on rigorous mathematical grounds and has been proven to be well posed³³. As for the boundary conditions, one has to fix the value g of the normal component of the field on the whole boundary S and the value λ of α on either the positive-polarity part S^+ of S (where $B_z > 0$) or on the negative-polarity part S^- (where $B_z < 0$). The XTRAPOL code²⁷ solves this problem by means of the iterative Grad–Rubin scheme:

$$\mathbf{B}^{(k)} \cdot \nabla \alpha^{(k)} = 0 \quad \text{in } \Omega \quad (4)$$

$$\alpha^{(k)} = \lambda \quad \text{on } S^+ \text{ or } S^- \quad (5)$$

$$\nabla \times \mathbf{B}^{(k+1)} = \alpha^{(k)} \mathbf{B}^{(k)} \quad \text{in } \Omega \quad (6)$$

$$\nabla \cdot \mathbf{B}^{(k+1)} = 0 \quad \text{in } \Omega \quad (7)$$

$$\mathbf{B}_n^{(k+1)} = g \quad \text{on } S \quad (8)$$

The initial field $\mathbf{B}^{(0)}$ is chosen to be the potential magnetic field \mathbf{B}_p with a normal component equal to g on S (by definition \mathbf{B}_p is current free, that is, $\nabla \times \mathbf{B}_p = 0$). XTRAPOL uses a finite-difference method with a representation of \mathbf{B} based on a vector potential \mathbf{A} (with a convenient choice of gauge), which ensures that $\nabla \cdot \mathbf{B} = 0$ to the accuracy of round-off errors. The elliptic part (equations (6)–(8)) for $\mathbf{B}^{(k+1)}$ is solved through a positive-definite linear system, and the hyperbolic part (equations (4)–(5)) for $\alpha^{(k)}$ is solved by transporting the values λ imposed on either S^+ or S^- along the magnetic field lines of $\mathbf{B}^{(k)}$. The code uses the message passive interface library. It provides a solution even if the photospheric flux is not balanced.

Magnetic data and boundary conditions. The boundary conditions needed by our method, g and λ , are extracted from the photospheric vector magnetograms obtained from the scans of the spectropolarimeter of the Solar Optical Telescope³⁴ on board the satellite Hinode¹⁷. More precisely, we used level-2 data (available online at <http://sot.lmsal.com/data/sot/level2d/>) obtained by applying the MERLIN inversion code³⁵ to the Stokes parameters I , Q , U and V measured by this instrument. The well-known 180° ambiguity suffered by the transverse component of the magnetic field is resolved by using the minimum-energy code (ME0) based on a recent re-implementation^{36,37} of the original method³⁸. By using standard transformation formulae³⁹, we have also converted the scales and the magnetic components from the observer frame to the Cartesian frame tangent to the solar surface and centred on the middle point of the vector magnetograms. We have chosen a sequence of four vector magnetograms covering the period from December 9, 10:00 UT, to December 12, 20:30 UT (the last available data before the eruption). Note that the raw data provided by the instrument are neither smoothed nor preprocessed.

The value of g is directly furnished by the data. That of λ is computed from the three components of the measured magnetic field \mathbf{B}^{phot} according to⁴⁰

$$\lambda = \frac{4\pi j_z^{\text{phot}}}{c B_z^{\text{phot}}} = \frac{(\nabla \times \mathbf{B}^{\text{phot}})_z}{B_z^{\text{phot}}}$$

where j_z^{phot} is the vertical component of the current density and c is the speed of light. To prevent unreliable values of λ near the polarity inversion line where B_z^{phot} is small, λ is set to zero if $|B_z^{\text{phot}}|$ is below a particular value, B_z^{cut} . A similar cut-off is used for the intensity of the tangential component B_t^{phot} of \mathbf{B} . This avoids unreliable values of j_z^{phot} due to sudden variations of B_t^{phot} below the noise level. It should be noted that some improvements leading to non-zero values of λ closer to the polarity inversion line could be obtained by applying further smoothing and interpolation on the computational mesh.

Magnetic environment properties. Using these boundary conditions, we compute the solutions of our reconstruction problem with a numerical resolution of $501 \times 331 \times 201$. The quality of the results is evaluated by calculating the standard a-posteriori diagnostics, which are found to be much better than those characterizing previous reconstructions^{18–21,41,42}. In particular, we obtain much smaller values for the angle between the magnetic field and the electric current density (3.73° versus 14.48° (model¹⁸ W_{pp}^+), these values being computed from the actual diagnostic CWsin, which deals with the sine of this angle) and for the functional L_f measuring the distance to a true equilibrium (0.07 G² Mm⁻² versus 2.27 G² Mm⁻² in ref. 19). Owing to our specific discretization alluded to above, the difference is even larger for the functionals measuring the residual divergence of the computed magnetic field. We obtain $L_d = 10^{-30}$ G² Mm⁻² versus $L_d = 1.15$ G² Mm⁻², from ref. 19, where the reconstructions were made by the optimization method and the constraint $\nabla \cdot \mathbf{B} = 0$ was not imposed a priori, the field being made only as ‘divergenceless’ as possible. Also, we obtain $\langle |f_i| \rangle = 2.7 \times 10^{-17}$ versus 3.6×10^{-8} for the best model¹⁸ W_{pp}^+ , where a Grad–Rubin scheme is used, but with a discretization leading to a non-zero resolution dependent value of $\nabla \cdot \mathbf{B}$ at each node. As another test, we have considered the difference between the measured values of α at the two ends of any magnetic line, which in principle should vanish if the boundary data are strictly compatible with the existence of a force-free field in Ω . We find that this quantity is relatively small for the field we compute despite the fact that our well-posed formulation uses only the values λ of α in the positive-polarity region. It in fact takes relatively large values for the reconstructions based on the use of all three components of the magnetic field on the whole active region.

We also calculate the free magnetic energy ΔW (that is, the difference between the magnetic energy of the solution and that of the associated current-free field \mathbf{B}_p) stored in the equilibria. This is a very important quantity to be compared with the energy released during the following X-class eruption. For our last computed pre-flare configuration, we find $\Delta W = 7 \times 10^{32}$ erg, which is above the upper limit of the estimate ((1.4–4.5) $\times 10^{32}$ erg) of the energy released during the flare²⁶. The good observational compatibility of this result can be taken as another indication of the quality of our reconstructions (in particular, we recall that having a low value of L_d is well known to be necessary for obtaining an accurate value of the energy⁴³). Note that the energies previously found^{18,19} ($\Delta W = 5 \times 10^{32}$ and 1.3×10^{32} erg) are also compatible with the energy release estimates, with the second value¹⁹ being close to the lower limit.

As noted above, it is important to reconstruct the coronal field by different methods and to check for the coherence of the results. We have also done reconstructions using a newly developed numerical code, MESHMH²⁸, which solves the equilibrium equations (4)–(8) in the whole spherical corona. It is an adaptive unstructured (tetrahedral) mesh code, which includes in particular a different scheme for computing α . This scheme solves a linear non-symmetric system using the GMRES algorithm⁴⁴. The boundary conditions are provided by composite photospheric data from three instruments: a Hinode/SOT vector magnetogram at the active region scale, a SOHO/MDI full-disk longitudinal magnetogram and a SOLIS synoptic

map with a latitude–longitude resolution of $1,368 \times 2,824$. As it is based on an unstructured mesh, MESHMHD can introduce high resolution where it is needed in the region and around the flux rope, and lower resolution elsewhere. As a striking result, we found that the two codes detect the presence of a twisted flux rope and capture its bifurcation to different anchoring points on the east side (Extended Data Fig. 2).

Prediction of the later evolution by using a dynamical MHD code. During the eruptive phase, the coronal magnetic field evolves according to its own internal dynamics and can then no longer be determined from its photospheric values. But we can use our dynamical MHD code METEOSOL³⁰, which solves the full system of MHD equations, to predict its evolution from the last computed pre-eruptive equilibrium state. We inject that state into the code as an initial condition and select boundary conditions able to describe the actual photospheric processes that force the field to evolve. In our previous theoretical studies^{3,4,45}, we identified three such processes and showed that each of them can trigger a flare and a CME:

- (1) Partial cancellation near the polarity inversion line⁴⁴.
- (2) Turbulent diffusion^{3,5,46}, which is an important process permanently acting on the whole surface of the Sun, where it leads to the continuous dispersion of active regions. It can be characterized by a coefficient of turbulent diffusion $\kappa_B = 10^{-3}$ or 10^{-4} .
- (3) Plasma motions that diverge from the two spots of a bipolar region and converge towards the polarity inversion line in its vicinity, into which they transport a part of the magnetic flux⁴. These ‘moat flows’, which have been observed in an active region^{47,48}, have their source just outside the penumbra, near the locus at which the Evershed flow disappears.

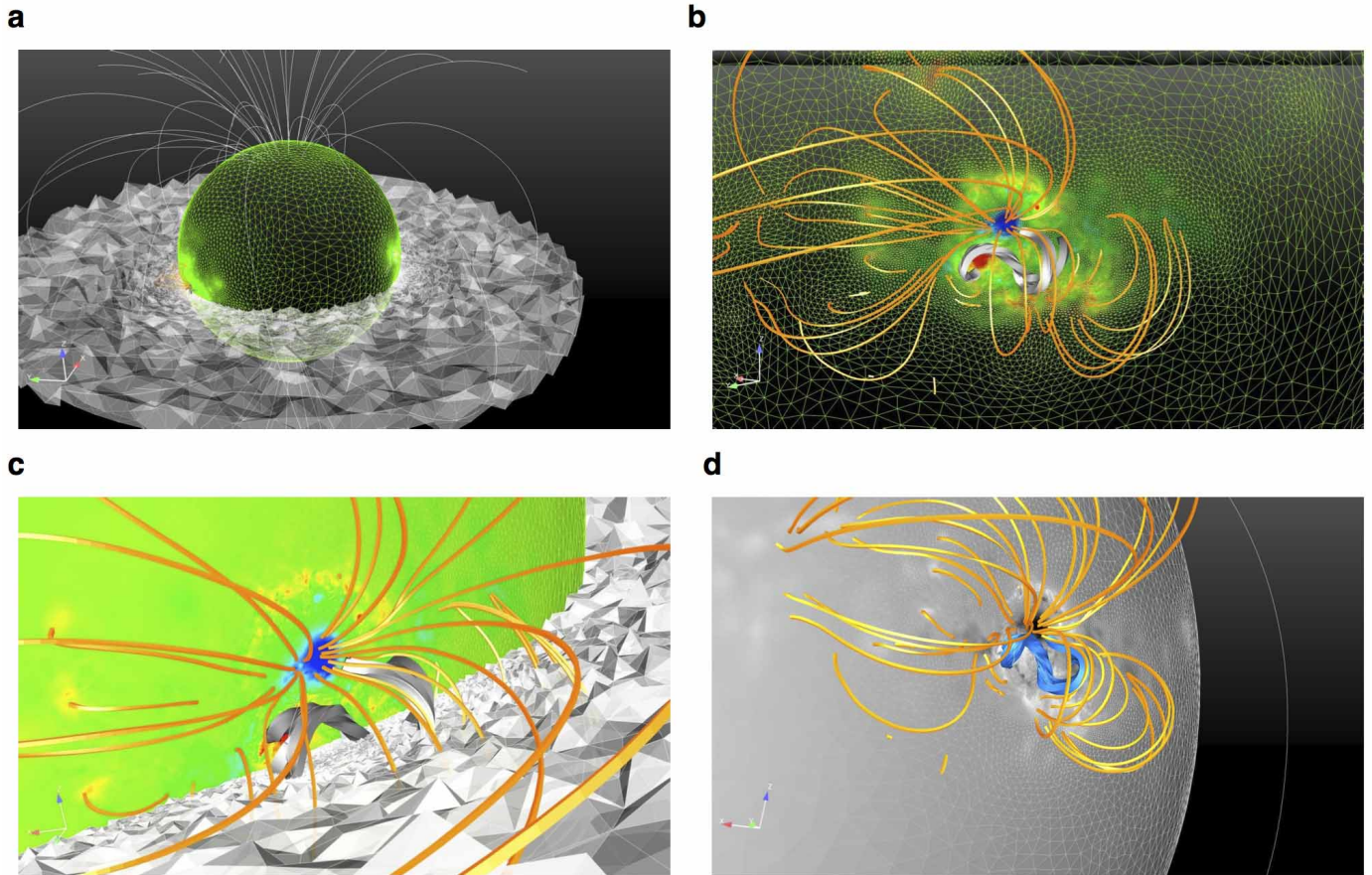
We successively compute three MHD evolutions, each starting from the same initial state and driven by one of the processes above. The processes are introduced into the code by requiring the tangential component of the electric field on S to assume a specific form.

The three types of boundary condition lead after a short interval to a major disruption. This is similar to what we obtained in the corresponding theoretical models previously developed. There is, however, an important difference: here the initial presence and properties of the twisted rope are no longer postulated, but are furnished by our environment model, which determines to a very good approximation the actual initial structure of the field above the active region. Reconstruction has shown the presence of a rope in an active region⁴⁹, but this has been rare. A striking result of our modelling is that the eruption is due to a loss of equilibrium occurring when the energy of the configuration becomes of the order of the energy of the partially open field B_{so} , defined below.

The partially open field. To define B_{so} , we first construct an additional magnetic field, the open field B_s , having the same normal component g on S as the evolving coronal field B . In contrast to the potential field B_p , whose most magnetic lines are closed (each one connects two points of S), B_s has all its field lines open (they connect S to the upper and lateral boundaries of the computational box). It is current free except on the surface separating outgoing lines from ingoing ones, across which it reverses. As with B_p , B_s is in equilibrium in the sense that it does not exert any force on the plasma in which it is embedded. We can also construct equilibrium fields, B'_s , satisfying the same boundary condition and ‘interpolating’ between B_p and B_s . These fields are only partially open—they have both closed and open lines—and they are also current free except on a reversal surface. The field B_{so} is one of

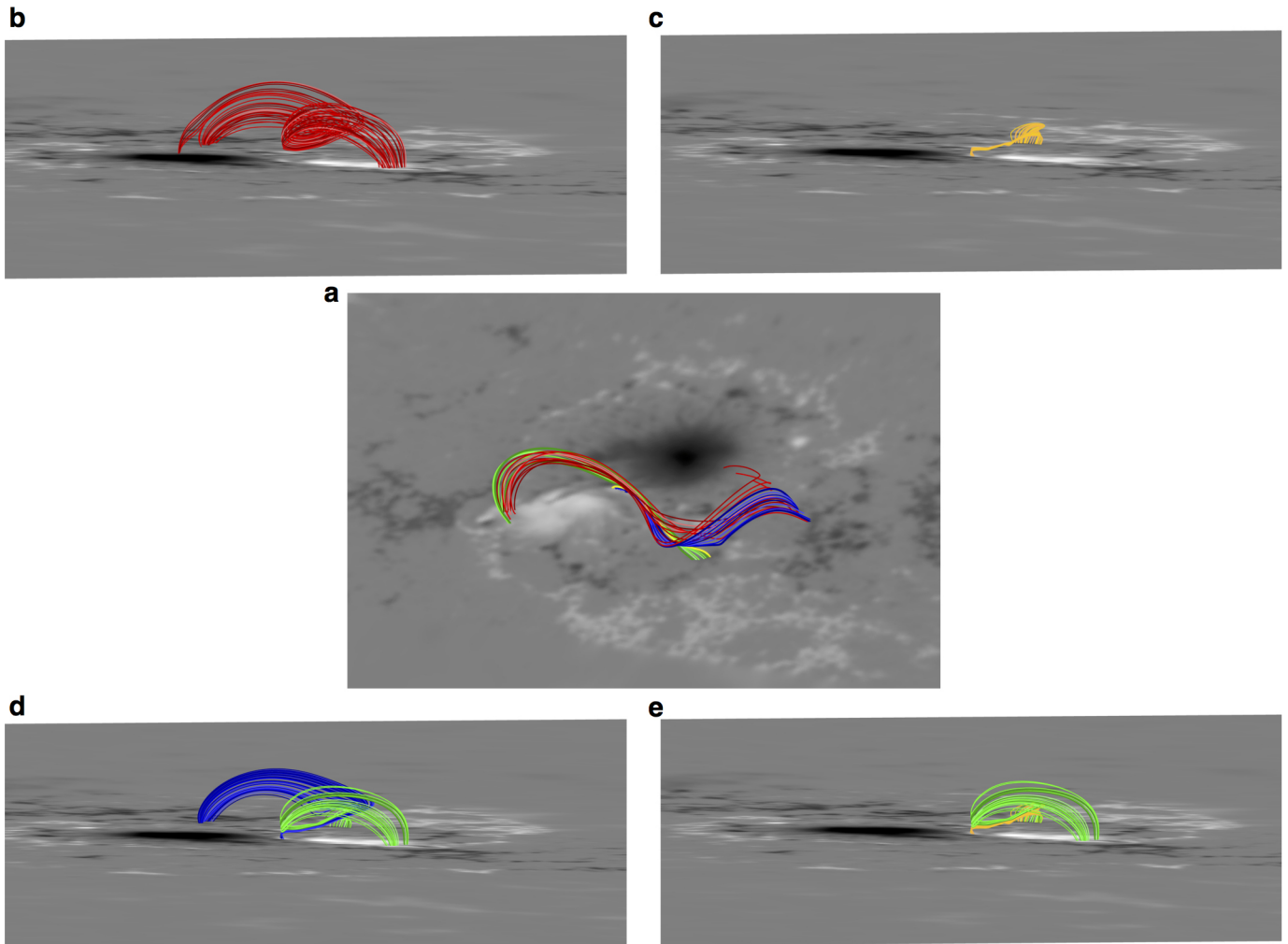
these fields B'_s . It is selected by requiring that its open lines connect to S in the region where the electric currents are concentrated. This field was first introduced in an analytical theory³¹ that describes the evolution of B as a sequence of equilibrium states, this quasi-static approximation being valid as long as the evolution is slow. It was argued on general grounds that $W(B) \leq W(B_{so}) \leq W(B'_s)$ (with $W(B)$ denoting the energy of B), and that B starts experiencing a fast expansion leading to its partial opening when $W(B)$ approaches $W(B_{so})$. Such fast evolution implies a breakdown of the quasi-static approximation and one needs to adopt the dynamical approach described in the previous item to get a proper description of it.

31. Aly, J.-J. & Amari, T. Structure and evolution of the solar coronal magnetic field. *Geophys. Astrophys. Fluid Dyn.* **101**, 249–287 (2007).
32. Wiegmann, T., Inhester, B. & Sakurai, T. Preprocessing of vector magnetograph data for a nonlinear force-free magnetic field reconstruction. *Sol. Phys.* **233**, 215–232 (2006).
33. Boulmezaoud, T. Z., & Amari, T. On the existence of non-linear force-free fields in three-dimensional domains. *Z. Angew. Math. Phys.* **51**, 942–967 (2000).
34. Tsuneta, S. *et al.* The Solar Optical Telescope for the Hinode mission: an overview. *Sol. Phys.* **249**, 167–196 (2008).
35. Skumanich, A. & Lites, B. W. Stokes profile analysis and vector magnetic fields. I - Inversion of photospheric lines. *Astrophys. J.* **322**, 473–482 (1987).
36. Leka, K. D. *et al.* Resolving the 180° ambiguity in solar vector magnetic field data: evaluating the effects of noise, spatial resolution, and method assumptions. *Sol. Phys.* **260**, 83–108 (2009).
37. Crouch, A. D., Barnes, G. & Leka, K. D. Resolving the azimuthal ambiguity in vector magnetogram data with the divergence-free condition: application to discrete data. *Sol. Phys.* **260**, 271–287 (2009).
38. Metcalf, T. R. Resolving the 180-degree ambiguity in vector magnetic field measurements: the ‘minimum’ energy solution. *Sol. Phys.* **155**, 235–242 (1994).
39. Allen Gary, G. & Hagyard, M. J. Transformation of vector magnetograms and the problems associated with the effects of perspective and the azimuthal ambiguity. *Sol. Phys.* **126**, 21–36 (1990).
40. Régnier, S., Amari, T. & Kersalé, E. 3D coronal magnetic field from vector magnetograms: non-constant-alpha force-free configuration of the active region NOAA 8151. *Astron. Astrophys.* **392**, 1119–1127 (2002).
41. Fan, Y.-L., Wang, H.-N., He, H. & Zhu, X.-S. Application of a data-driven simulation method to the reconstruction of the coronal magnetic field. *Res. Astron. Astrophys.* **12**, 563–572 (2012).
42. Inoue, S. *et al.* Buildup and release of magnetic twist during the X3.4 solar flare of 2006 December 13. *Astrophys. J.* **760**, 17 (2012).
43. Valori, G., Démoulin, P., Parlat, E. & Masson, S. Accuracy of magnetic energy computations. *Astron. Astrophys.* **553**, A38 (2013).
44. Saad, Y. & Schultz, M. H. GMRES: a generalized minimal residual algorithm for solving non symmetric linear systems. *SIAM J. Sci. Stat. Comput.* **7**, 856–869 (1986).
45. Amari, T., Aly, J.-J., Luciani, J.-F., Mikic, Z. & Linker, J. Coronal mass ejection initiation: on the nature of the flux cancellation model. *Astrophys. J.* **717**, L26 (2010).
46. Wang, Y. M., Sheeley, N. R. & Nash, A. G. A new solar cycle model including meridional circulation. *Astrophys. J.* **383**, 431–442 (1991).
47. Chae, J. *et al.* The formation of a prominence in active region NOAA 8668. I. SOHO/MDI observations of magnetic field evolution. *Astrophys. J.* **560**, 476–489 (2001).
48. Lites, B. W., Socas-Navarro, H., Skumanich, A. & Shimizu, T. Converging flows in the penumbra of a δ sunspot. *Astrophys. J.* **575**, 1131–1143 (2002).
49. Yan, Y. *et al.* The magnetic rope structure and associated energetic processes in the 2000 July 14 solar flare. *Astrophys. J.* **551**, L115–L119 (2001).



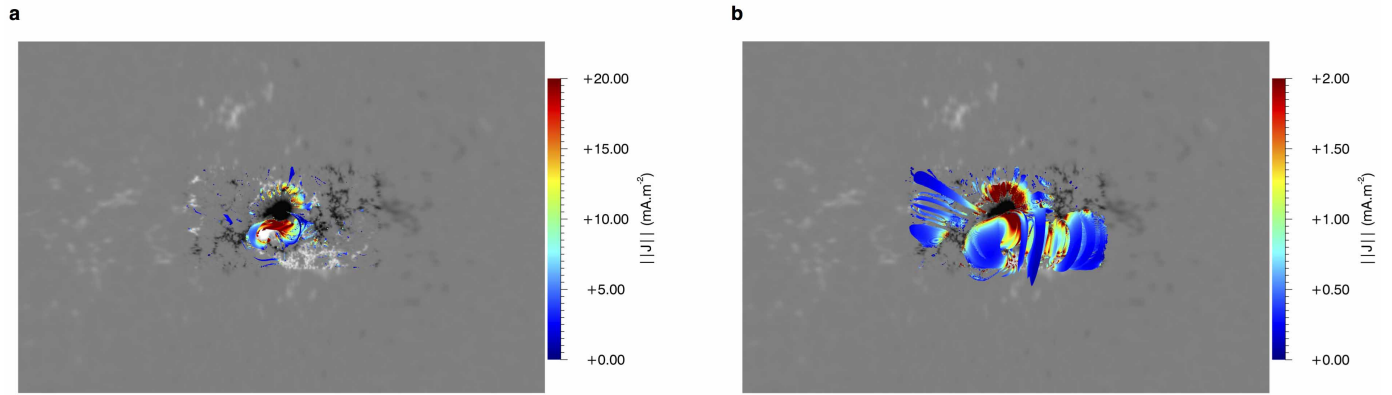
Extended Data Figure 1 | Another multiscale model. Full-Sun magnetic configuration obtained using composite data set (Hinode/SOT and SOLIS synoptic map) and the state-of-the-art numerical code MESHMHD, which is a tetrahedral adaptive-mesh equilibrium code. Local and global scales are both accessible using very high-resolution data around the active region and lower resolution elsewhere. The twisted rope obtained with XTRAPOL is fully recovered. **a**, Global view showing the disk of tetrahedral-cell mesh and the spherical photosphere, where we have indicated the various resolutions for the

northern hemisphere and, in transparency behind the disk, for the southern hemisphere. **b**, Zoom onto the active region showing the high resolution used around it. **c**, Closer look at the rope, with a cut showing how the adaptive scheme allows high mesh resolution in the regions where the coronal electric current and magnetic field are stronger. **d**, Another point of view, exhibiting the large extent of the rope, which is still confined by the overlying field lines (orange).



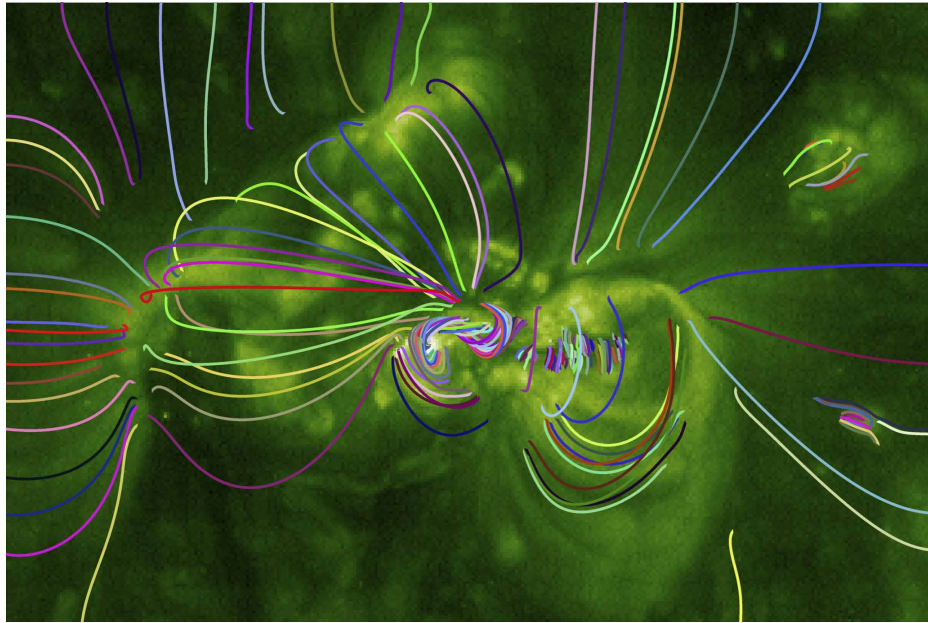
Extended Data Figure 2 | Hyperbolic flux tube. **a**, Breaking of the twisted rope into various components to exhibit its hyperbolic nature, using the same colour code as in Fig. 1. **b**, Core of the rope, which is highly twisted (by about 2.25π). **c**, Underlying highly sheared arcades below the core. **d**, Two

J-shaped arcades whose central parts become tangential to each other. **e**, One of the J-shaped set of loops (green) above the sheared arcades (yellow), becoming tangential to each other near the neutral line.



Extended Data Figure 3 | Signature of the pre-eruptive current density of the reconstructed magnetic configuration of 12 December, 20:30 UT. We have plotted here two isosurfaces of the force-free function α measuring the ratio of the electric current density to the magnetic field: **a**, $\alpha = -0.23 \text{ Mm}^{-1}$; **b**, $\alpha = -0.05 \text{ Mm}^{-1}$. These isosurfaces are coloured according to the values of

the modulus of the current density, $|j|$. The large-scale structure of the twisted rope (and of small parts above) is well exhibited by this quantity α in **a**, in agreement with Fig. 2b, whereas weaker electric currents (overlying) structures are shown in **b**.



Extended Data Figure 4 | Extreme-ultraviolet emission and magnetic structure. Selected field lines of the reconstructed magnetic configuration of 12 December, 20:30 UT, overlaid on an SOHO/EIT extreme-ultraviolet emission image taken at 23:49 UT. The emission is well correlated with the

magnetic lines in the region of the twisted rope and in the regions of approximately current-free loops, such as that located on the right-hand side of the rope.